communications physics

Article

https://doi.org/10.1038/s42005-024-01686-7

Ultrafast opto-magnetic effects in the extreme ultraviolet spectral range

Martin Hennecke[1] ✉, Clemens von Korff Schmising[1], Kelvin Yao[1], Emmanuelle Jal[2], Boris Vodungbo[2], Valentin Chardonnet[2], Katherine Légaré[3], Flavio Capotondi[4], Denys Naumenko[4], Emanuele Pedersoli[4], Ignacio Lopez-Quintas[4,5], Ivaylo P. Nikolov[4], Lorenzo Raimondi[4], Giovanni De Ninno[4,6], Leandro Salemi[7], Sergiu Ruta[8,9], Roy Chantrell[8], Thomas Ostler[10], Bastian Pfau[1], Dieter Engel[1], Peter M. Oppeneer[7], Stefan Eisebitt[1,11] & Ilie Radu[1,12] ✉

Coherent light-matter interactions mediated by opto-magnetic phenomena like the inverse Faraday effect (IFE) are expected to provide a non-thermal pathway for ultrafast manipulation of magnetism on timescales as short as the excitation pulse itself. As the IFE scales with the spin-orbit coupling strength of the involved electronic states, photo-exciting the strongly spin-orbit coupled core-level electrons in magnetic materials appears as an appealing method to transiently generate large opto-magnetic moments. Here, we investigate this scenario in a ferrimagnetic GdFeCo alloy by using intense and circularly polarized pulses of extreme ultraviolet radiation. Our results reveal ultrafast and strong helicity-dependent magnetic effects which are in line with the characteristic fingerprints of an IFE, corroborated by ab initio opto-magnetic IFE theory and atomistic spin dynamics simulations.

Light-driven ultrafast magnetic phenomena occurring on ever faster and smaller time and length scales are at the core of the modern magnetism research[1,2]. A long sought-after and yet to be realized phenomenon is the coherent and deterministic control of a macroscopically ordered spin ensemble on the sub-cycle timescales of the photo-exciting laser field[3,4]. In this context, one of the most prominent effects that could lead to large, ultrafast changes of magnetization is the inverse Faraday effect (IFE). Discovered originally in paramagnetic solids[5], the IFE was shown to generate an effective magnetic field or, equivalently, an induced magnetic moment in a medium upon photoexcitation with circularly polarized light pulses. According to classical IFE theory[5], the orientation and the magnitude of the light-induced magnetic moment are respectively determined by the helicity of circularly polarized light (or its angular momentum) and the combined effect of the magneto-optical susceptibility of the photo-excited medium and the incident light intensity. In case of metallic ferro- or antiferromagnetic materials, a fully ab initio quantum-mechanical treatment of the IFE has revealed that its action on these materials is significantly different compared to the originally discovered effect, predicting a complex dependence of the IFE-induced magnetization on both helicity and wavelength, which is not covered anymore by the conventional theory[6–8]. However, the high absorption of the optical excitation in these materials typically leads to strong heat-induced demagnetization which hinders the observation of any potential non-thermally induced magnetization[9]. Thus, the actual influence of an IFE on the sub-picosecond spin dynamics observed in such systems as, for example, all-optical switching phenomena in ferrimagnetic rare-earth transition-metal alloys like GdFeCo[10–13], remains highly debated and elusive so far[14].

The magnitude of the IFE depends on the light intensity and its polarization, as well as on the spin-orbit coupling (SOC) of the involved electronic states via the wavelength- and helicity-dependent opto-magnetic constant $\mathcal{K}^{\mathrm{IFE}}_{\sigma_\pm}(\omega)$[6,8]:

$$\vec{M}_{\mathrm{ind}}(\omega) = i\,\mathcal{K}^{\mathrm{IFE}}_{\sigma_\pm}(\omega)\left[\vec{E}(\omega)\times\vec{E}^{*}(\omega)\right] \tag{1}$$

[1]Max-Born-Institut für Nichtlineare Optik und Kurzzeitspektroskopie, Max-Born-Straße 2A, 12489 Berlin, Germany. [2]Sorbonne Université, CNRS, Laboratoire de Chimie Physique – Matière et Rayonnement, LCPMR, 75005 Paris, France. [3]Institut National de la Recherche Scientifique, INRS-EMT, Varennes, QC J3X 1P7, Canada. [4]FERMI, Elettra-Sincrotrone Trieste, 34149 Basovizza, Trieste, Italy. [5]Grupo de Investigación en Aplicaciones del Láser y Fotónica, Departamento de Física Aplicada, University of Salamanca, 37008 Salamanca, Spain. [6]Laboratory of Quantum Optics, University of Nova Gorica, 5001 Nova Gorica, Slovenia. [7]Department of Physics and Astronomy, Uppsala University, P.O. Box 516, SE-751 20 Uppsala, Sweden. [8]Department of Physics, University of York, York YO10 5DD, UK. [9]College of Business, Technology and Engineering, Sheffield Hallam University, Howard Street, Sheffield S1 1WB, UK. [10]Department of Physics and Mathematics, University of Hull, Cottingham Road, Hull HU6 7RX, UK. [11]Institut für Optik und Atomare Physik, Technische Universität Berlin, Straße des 17. Juni 135, 10623 Berlin, Germany. [12]European X-ray Free-Electron Laser, Holzkoppel 4, 22869 Schenefeld, Germany. ✉e-mail: hennecke@mbi-berlin.de; ilie.radu@xfel.eu

where $\vec{E}(\omega)$ denotes the light electric field, $\sigma_{\pm}$ its helicity, and $\vec{M}_{\mathrm{ind}}$ the induced magnetization along the $\vec{k}$ vector of the incident circularly polarized light beam. The IFE, which is an electronic Raman process, has thus far been investigated theoretically[6,8,15–18], but a direct comparison with measurements is lacking. A potential way of generating strong opto-magnetic interactions in metallic magnets is the excitation of core-level electrons, involving states with much higher SOC compared to the valence band (e.g., 1.1 eV vs. 65 meV in case of Fe 3p and 3d electrons, respectively[19]) that can be accessed by short wavelength radiation in the extreme ultraviolet (XUV) or soft x-ray range. The availability of free-electron lasers (FEL) providing femtosecond pulses of very high brilliance with control over the light polarization has enabled studies of x-ray induced magnetization dynamics, extending the capabilities from element-specific probing, employing, e.g., the x-ray magnetic circular dichroism (XMCD), towards element-specific excitation of highly non-equilibrium states[20–24]. However, besides first theoretical predictions, there is, to the best of our knowledge, no experimental evidence available so far on the existence of opto-magnetic effects like the IFE at these XUV wavelengths.

In this work, we study the ultrafast magnetization dynamics of ferrimagnetic GdFeCo alloy induced by photoexcitation with intense femtosecond circularly polarized pulses in the XUV spectral range generated by the free-electron laser FERMI. Comparing the helicity-dependent dynamics upon on- and off-resonant excitation with respect to the Fe $M_{3,2}$ resonance, we find strong dynamic helicity- and wavelength-dependent effects that resemble the expected characteristics of an IFE. Analyzing the magnitude and wavelength-dependence of the observed effect, we can rule out a thermal origin caused by dichroic absorption due to the XMCD. This finding is corroborated by atomistic spin dynamics (ASD) simulations, revealing that even in case of fully on-resonant excitation, the expected XMCD response is up to an order of magnitude smaller compared to the observed effect. Instead, we find qualitative agreement with ab initio calculations of the IFE in the XUV spectral range. Our results thus identify the existence of an IFE in the XUV spectral range.

Results and discussion

Time-resolved pump – probe measurements

The experimental concept employing the XUV pump − magneto-optics probe technique to trigger and measure the IFE is depicted in Fig. 1a. The sample was excited at normal incidence using ≈90 fs (full width at half maximum, FWHM) XUV pulses of variable polarization [circular right/left ($\sigma_{\pm}$) and linear horizontal (lin. hor.)], tuned to photon energies around the Fe $M_{3,2}$ resonance. The XUV-induced dynamics were probed under 45° by linearly polarized ≈90 fs (FWHM) optical pulses at 400 nm wavelength, measuring both the magneto-optical Faraday rotation in transmission and the Kerr rotation in reflection, obtaining magnetic contrast by flipping an out-of-plane saturating magnetic field of ±8 mT applied to the sample.

Figure 1b shows the XUV absorption spectra (XAS) measured on the GdFeCo sample across the Fe $M_{3,2}$ resonance for opposite magnetic fields and the resulting XMCD spectrum. The absorption peak at around 56.1 eV corresponds to the resonant excitation of 3p electrons of Fe into 3d states; the second and less pronounced peak around 62.0 eV arises due to resonant excitation of the small fraction of Co atoms. Note that the vanishing XMCD at this photon energy results from the superposition of bipolar XMCD features of the Fe and Co $M_{3,2}$ resonances weighted by their different concentrations in the alloy (compare Supplementary Fig. 8). To study the wavelength-dependence of the XUV excitation across the Fe $M_{3,2}$ resonance, the photon energy of the FEL pulses was tuned to fixed positions in the spectrum at 51.0 eV (below resonance), 54.1 eV (largest XMCD), 56.1 eV (highest absorption) and 64.0 eV (above resonance).

Figure 2 shows the temporal evolution of magnetization after resonant excitation by linearly and circularly polarized XUV pulses at a photon energy of 54.1 eV, as measured by the Faraday signal; for the Kerr measurements leading to similar results, see Supplementary Note 3. The data was fitted using a double-exponential fit function convoluted with a Gaussian (solid lines in Fig. 2), taking into account the ultrafast demagnetization, the subsequent relaxation process and the experimental time resolution of ≈280 fs. For clarity, the pump-probe scans are displayed only for two incident XUV fluences, showing the dynamics upon low and high fluence excitation. The data reveals a clear influence of the XUV polarization on the demagnetization amplitudes, emerging upon excitation with increasing incident fluence (compare 1.3 and 6.7 mJ/cm^2). Above 1.3 mJ/cm^2, the XUV pump helicity drives either an enhancement or a decrease of the demagnetization effect that takes place within the first hundreds of femtoseconds; this helicity-dependent difference in demagnetization magnitudes lasts for tens of picoseconds, i.e., also during the magnetization relaxation process, emphasizing the strength and robustness of the transient XUV-induced magnetization. Such a helicity-dependent behavior is at variance with the case of linearly polarized XUV excitation that generates demagnetization based on purely thermal effects, i.e., demagnetization driven by ultrafast electronic heating.

Fluence- and wavelength-dependence

In Fig. 3, the demagnetization amplitudes obtained from the double-exponential fits are shown as a function of XUV photon energy, polarization, and incident excitation fluence, evaluated for the full range of used XUV fluences. The data reveals a strong helicity-dependent effect that is present over the whole range of photon energies used for excitation, be it on- (54.1 and 56.1 eV) or off-resonant (51.0 and 64.0 eV) with respect to the Fe $M_{3,2}$ resonance. The splitting between either enhanced or attenuated demagnetization amplitudes upon $\sigma_{\pm}$-polarized excitation ($D = 1 - \min[M/M_0]$, Fig. 3a) and accordingly the magnitude and sign of the difference ($\Delta M = D[\sigma_-] - D[\sigma_+]$, Fig. 3b) show that the effect is wavelength-dependent, clearly changing its polarity along the resonance. The data further reveals that the effect is strongly fluence-dependent; within the experimental uncertainty, two fluence regimes become apparent (illustrated by the white/gray shaded background in Fig. 3b) where the magnitude of ΔM initially increases with XUV fluence and then either reaches a saturated state at a constant ΔM value or decreases again as the fluence is further elevated. In case of below- and above-resonant excitation (51.0 and 64.0 eV), ΔM scales linearly with the fluence until the saturated state is achieved. It thereby reaches up to (32.2 ± 0.7) % difference in pump-induced change with respect to the equilibrium magnetization (largest ΔM observed for 5.3 mJ/cm^2 at 64.0 eV). In case of resonant excitation (54.1 and 56.1 eV), the data reveals a more complex fluence-dependence, indicating either a threshold-like behavior (54.1 eV) or even a fluence-dependent sign change of ΔM (56.1 eV). For excitation between 54.1 and 64.0 eV, the demagnetization reaches amplitudes of up to ≈100% at high fluences (depending on the helicity), corresponding to full demagnetization of the magnetic layer. This leads to the observed saturation or even quenching of ΔM in the high fluence regime, as the increasing thermal load and demagnetization starts to counteract the helicity-dependent effect (gray shaded regions).

The most striking observation is the presence of strong helicity-dependent differences even for the off-resonant excitation at photon energies where the XUV spectroscopy shows very small or even zero XMCD (compare Fig. 1b for 51.0 and 64.0 eV). In general, the XMCD provides a potential source of helicity-dependent dynamics due to the interaction of circularly polarized XUV pulses and the angular momentum of the excited electrons leading to a polarization-dependence of the absorbed fluence. This dichroic absorption effect would manifest in a different amount of thermally induced demagnetization, depending on the helicity of the XUV excitation pulse. However, due to the lack of sizeable dichroic absorption in case of 51.0 and 64.0 eV (compare Fig. 1b), this mechanism can already be ruled out as the driving force behind the observed helicity-dependence at these two photon energies, which strongly indicates the existence of an opto-magnetic effect such as the IFE. This interpretation is further corroborated by the linear scaling with the fluence (XUV intensity) observed at 51.0 and 64.0 eV (white shaded regions in Fig. 3b), resembling a typical IFE feature, since the magnetization induced by the IFE depends linearly on the incident light intensity via the opto-magnetic, wavelength-dependent constant (see Eq. 1

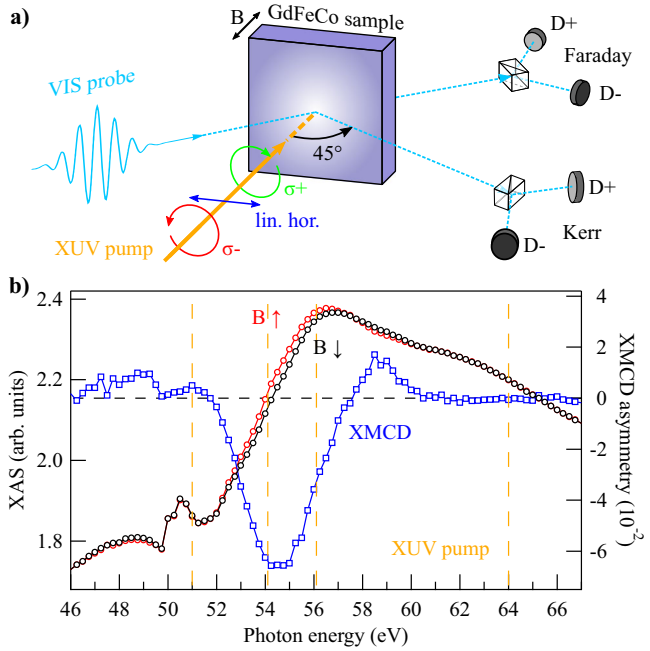

Fig. 1 | Experimental concept and spectroscopy. a Schematic of the time-resolved pump-probe experiment implemented at FERMI. The GdFeCo sample is excited using extreme ultraviolet (XUV) pump pulses with variable polarization (circular polarization with opposite helicity $\sigma_{\pm}$ and linear horizontal). The visible (VIS) light pulses probe the magneto-optical Faraday and Kerr rotation using a balanced photodetection scheme, consisting of a Wollaston prism and two photodiodes ($D_{\pm}$). Magnetic contrast is obtained by flipping an out-of-plane magnetic field (B) applied to the sample. **b** Static XUV absorption (XAS, red and black circles for opposite magnetic fields, left scale) and x-ray magnetic circular dichroism (XMCD) asymmetry spectra (blue squares, right scale) of the GdFeCo sample measured across the Fe $M_{3,2}$ resonance. The yellow dashed lines indicate the photon energies used for XUV pumping (51.0, 54.1, 56.1 and 64.0 eV). The static spectroscopy was carried out with an energy resolution of ≤0.01 eV using the ALICE reflectometer[41] at the PM3 beamline of BESSY II[42].

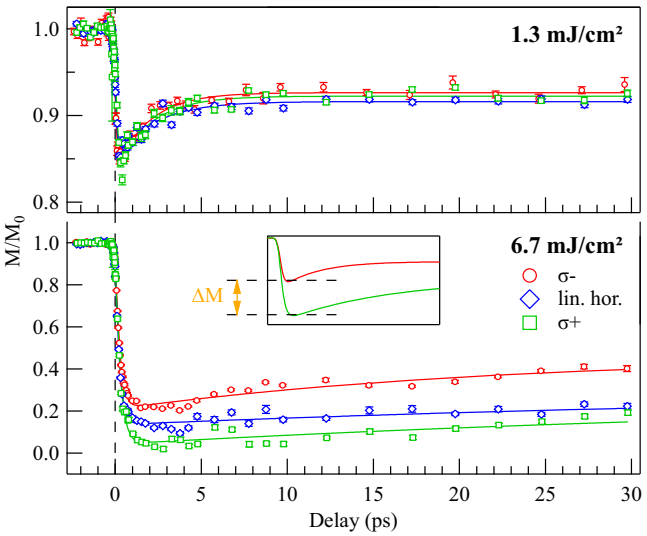

Fig. 2 | Time-resolved and helicity-dependent dynamics. Magnetization dynamics induced by fs extreme ultraviolet (XUV) pulses with variable polarization (circular polarization with opposite helicities $\sigma_{\pm}$, red circles and green squares, and linear horizontal polarization, blue diamonds) for two different fluences 1.3 and 6.7 mJ/cm^2 at 54.1 eV photon energy, i.e., at the maximum x-ray magnetic circular dichroism (XMCD) effect – see Fig. 1b. The magnetization is normalized to the equilibrium magnetization in the unexcited state (M/M_0). The solid lines correspond to double-exponential fits – see also Supplementary Note 2, where the complete set of fit parameters is provided. The data sets measured for the full range of XUV fluences as well as the time-resolved differences between the magnetization transients obtained for $\sigma_{\pm}$-polarized excitation are shown in Supplementary Figs. 3 and 4. The inset depicts how the helicity-dependent demagnetization amplitudes and their difference ΔM are obtained. The error bars are calculated as the standard error of the mean.

and Battiato et al.[8]). A possible explanation for the more complex fluence-dependence and the deviation from a purely linear scaling observed at 54.1 and 56.1 eV can be given by the steep slope of the XAS and XMCD spectra (see Fig. 1b) at these photon energies, significantly changing the response of the system when the spectrum is slightly reshaped or shifted while the system is driven out of equilibrium, depending on the strength of the excitation[25,26].

The generation of helicity-dependent effects that are longer-lived compared to the duration of the driving pump pulse (see Fig. 2) have been previously reported in various experimental studies of the IFE on different materials[9,13,15,27–29]. Although the IFE is active only during the pump pulse duration, the subsequent magnetization evolution is affected on much longer time scales, especially, when the impulsively IFE-induced magnetization is large (here we reach a maximum of ≈30% of the ground-state M_0 values) and, consequently, the system needs longer times to accommodate such large magnetic changes. Particularly for high fluence excitation, the helicity-dependent effects therefore persist until the end of the pump-probe delay range (−2.2 to 30 ps) scanned in the experiment (for a full set of time traces as a function of fluence, see Supplementary Fig. 4 and Supplementary Note 2).

Ab initio calculations of the inverse Faraday effect

To compare our experimental results to theoretical predictions of an opto-magnetic effect in the XUV spectral range, we carried out first ab initio calculations of the IFE[6,8] in vicinity of the Fe $M_{3,2}$ resonance. To reduce the computational complexity, the system was modeled as a stoichiometric $GdFe_2Co$ unit cell, focusing on the static opto-magnetic response for left (σ_-) and right (σ_+) circularly polarized excitation. The difference $\Delta_{\mathrm{IFE}} = \mathcal{K}^{\mathrm{IFE}}_{\sigma_-}(\omega) - \mathcal{K}^{\mathrm{IFE}}_{\sigma_+}(\omega)$ between the calculated opto-magnetic constants is shown in Fig. 4 (right axis) in comparison to the largest helicity-dependent effects that were experimentally observed for the studied excitation photon energies (left axis, see also Fig. 3b). Note that this comparison is purely qualitative, as it is based on two non-equivalent quantities, namely the difference between the static opto-magnetic constants vs. the transient demagnetization amplitudes obtained at a certain time after excitation. A fully quantitative comparison cannot be made yet, as the constants $\mathcal{K}^{\mathrm{IFE}}_{\sigma_\pm}(\omega)$ are obtained from stationary IFE calculations, so far not taking into account the fluence-dependent, non-equilibrium state present upon femtosecond excitation. To obtain a qualitative agreement with the experimental data, the calculated spectrum of the IFE response had to be shifted by +2.5 eV, which can be attributed to the effect of the core holes that is not included in the calculations[30–32] (see also the Methods section). The calculations support our experimental findings regarding the existence of an opto-magnetic effect at these wavelengths by predicting a highly wavelength-dependent IFE in vicinity of the $M_{3,2}$ resonance. The calculated Δ_{IFE} reverses its sign going through the resonance, which is again in qualitative agreement to the different polarity of ΔM observed in the experiment for below- and above-resonant excitation. This sign reversal occurs because the IFE spectra $\mathcal{K}^{\mathrm{IFE}}_{\sigma_-}(\omega)$ and $\mathcal{K}^{\mathrm{IFE}}_{\sigma_+}(\omega)$ display an energy shift with respect to each other at the 3p → 3d resonance, generated by the exchange splitting of the 3d states. The very steep slope of the Δ_{IFE} spectrum around the sign reversal thereby coincides with the fluence-dependent sign change of the helicity-dependent effect ΔM observed for 56.1 eV excitation. As mentioned before, even a small but ultrafast spectral shift of the Fe $M_{3,2}$ resonance, which has been experimentally observed[25,26] for laser-driven non-equilibrium states in similar magnetic materials, can lead to a sign reversal of the IFE depending on the excitation fluence. Furthermore, it

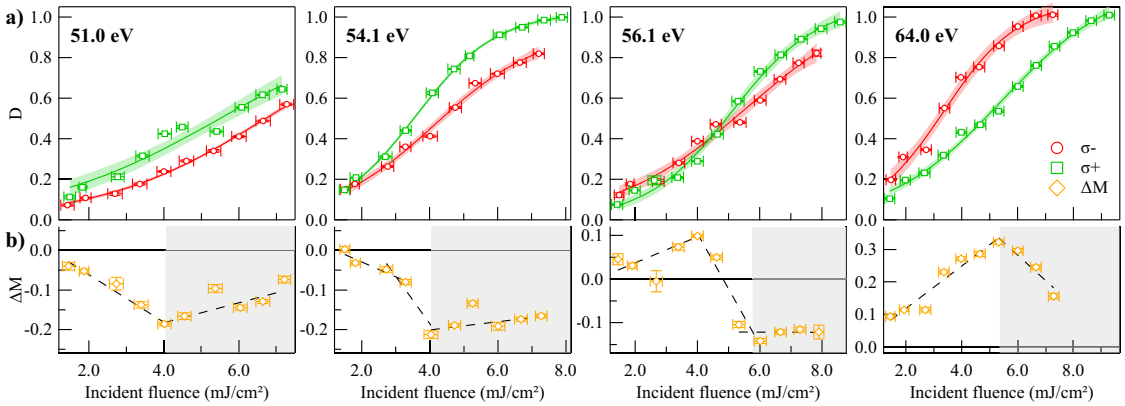

Fig. 3 | Fluence-dependence of the helicity-dependent dynamics. **a** Demagnetization amplitudes (D) measured upon pumping with circularly polarized extreme ultraviolet (XUV) pulses with opposite helicities ($\sigma_{\pm}$, red circles and green squares) and (**b**) their difference ΔM (yellow diamonds) as a function of incident fluence and XUV photon energy. All values are normalized to the magnetization in the unexcited state and ΔM was obtained as shown in the inset of Fig. 2. The solid lines in (**a**) correspond to sigmoid functions fitted as guide to the eye; the shaded areas denote the experimental uncertainty by a 90% confidence interval. The dashed lines in (**b**) indicate linear trends fitted to the different fluence regimes, in which the magnitude of the helicity-dependence ΔM increases upon increasing the XUV fluence and subsequently saturates or even decreases for high fluences (white and gray shaded background). For clarity, only the fluence-dependence of the $\sigma_{\pm}$-polarized excitation is shown (for linear polarization, see Supplementary Fig. 6). The error bars of the D values correspond to the uncertainty of the fitted demagnetization amplitudes (y-axis) and the standard error of the mean fluence values obtained by sorting the data after the free-electron laser (FEL) pulse energy (x-axis). The error bars of the ΔM values are calculated from the error propagation.

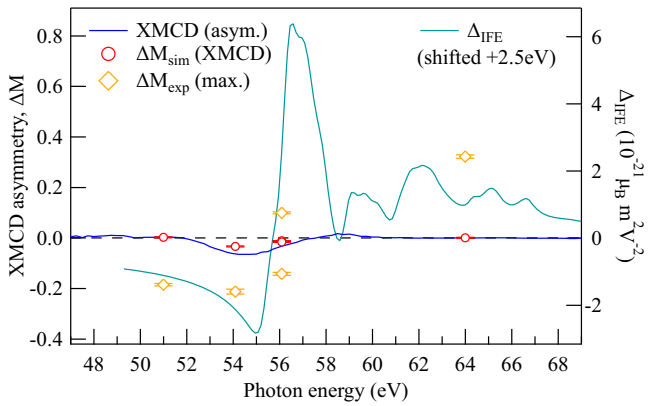

Fig. 4 | Comparison of experiment and theory. Qualitative comparison of the experimentally observed difference in demagnetization amplitudes ΔM_{exp} (yellow diamonds, left scale) to the difference Δ_{IFE} (turquoise line, right scale) between the calculated opto-magnetic constants $K^{IFE}_{\sigma_{\pm}}(\omega)$ obtained from ab initio inverse Faraday effect (IFE) theory. The red circles (left scale) correspond to the output of atomistic spin dynamics (ASD) simulations, simulating the expected demagnetization difference ΔM_{sim} induced by dichroic absorption due to the x-ray magnetic circular dichroism effect (XMCD, blue line). At 56.1 eV, two values are shown for ΔM_{exp}, reflecting its opposite polarity in the low vs. high fluence regime, which coincides with the steep slope of the Δ_{IFE} spectrum at this photon energy. The error bars of ΔM_{sim} reflect the uncertainty of the static XMCD characterization and ASD simulations, corresponding to the standard deviation of different simulation runs for a ± 0.5% variation of the input values of the XMCD magnitude. The error bars of ΔM_{exp} are calculated from the error propagation of the demagnetization amplitudes shown in Fig. 3.

has to be emphasized that the calculations show a finite response at the photon energies 51.0 and 64.0 eV, corroborating the existence of a helicity-dependent interaction at photon energies where a thermal mechanism due to the XMCD effect could already be ruled out. However, the calculations are so far not able to quantitatively explain the experimental results regarding the magnitude of the observed helicity-dependence. Although the XAS show only a minor contribution due to the small amount of Co in the alloy (compare Fig. 1b at ≈62.0 eV), the IFE calculations show a finite extension of the opto-magnetic response up to the Co $M_{3,2}$ resonance, which can qualitatively explain the observation of helicity-dependent effects at 64.0 eV, but not yet the relatively large magnitude of the effect compared to the Fe response.

Atomistic spin dynamics simulations

In case of fully resonant excitation at 54.1 and 56.1 eV, the observed helicity-dependence could further result from the combined action of an IFE together with the dichroic absorption caused by the finite XMCD present at these photon energies (compare Fig. 1b). To quantify the actually expected effect of the XMCD on the helicity-dependent dynamics, atomistic spin dynamics (ASD) simulations were carried out[11,33–35], simulating the influence of the dichroic absorption on the helicity-dependent demagnetization amplitudes (see Fig. 4). For best comparability, the excitation fluence was calibrated between experiment and simulation by matching the demagnetization amplitudes obtained upon linearly polarized excitation. While the absence of any helicity-dependence in the XMCD-driven ASD simulations is obvious for photon energies without XMCD (51.0 and 64.0 eV), the simulation shows that even in the fully resonant case (54.1 and 56.1 eV), the expected dichroic demagnetization effects would be smaller by at least a factor of six (comparing ΔM_{sim} and ΔM_{exp} at 54.1 eV) and by almost an order of magnitude compared to the largest effect observed across the spectrum. Thus, a significant contribution of a purely thermal mechanism (via dichroic absorption) on the observed helicity-dependent dynamics can be ruled out, strengthening our conclusions regarding the existence of an opto-magnetic effect like the IFE for both on- and off-resonant excitation in vicinity of the Fe $M_{3,2}$ resonance.

Conclusions

In conclusion, we studied the impact of femtosecond XUV photoexcitation of a ferrimagnetic GdFeCo layer using circularly polarized FEL pulses at the Fe $M_{3,2}$ resonance. The systematic investigation of time-resolved magneto-optical Faraday rotation data obtained as a function of XUV excitation fluence, photon energy and polarization reveals a strong and long-lived helicity-dependent effect on the ultrafast demagnetization dynamics. The analysis of its wavelength- and fluence-dependence in comparison to static XMCD spectroscopy and time-resolved ASD simulations shows that the observed effect cannot be induced by the XMCD, i.e., thermally due to dichroic absorption. Instead, it has the characteristic fingerprints of an opto-magnetic effect, which is further corroborated by first ab initio theory on the IFE at the Fe $M_{3,2}$ resonance, showing qualitative agreement between the

calculated IFE spectrum and the experimental data. Further experimental studies and theoretical efforts are needed for obtaining a quantitative understanding of the experimental results, especially with respect to the non-trivial fluence-dependence observed for excitation on the XUV resonance. This requires considering the IFE also in the highly non-equilibrium state upon femtosecond pulsed excitation, which is currently not included in the ab initio opto-magnetic theory. Complementary measurements upon resonant excitation of the Fe L edges, exciting 2p core-level electrons with even larger SOC compared to the 3p states, would provide further insights into the actual scaling of the IFE with the SOC and photon energy. Modern x-ray free-electron lasers can provide the required highly intense, circularly polarized femtosecond pulses of soft x-rays[20,36,37]. The observation of large opto-magnetic effects in the XUV spectral range also implies a significant, yet to be explored impact on ultrafast magnetization switching phenomena in addition to the MCD-induced helicity-dependence known from the visible-light regime[38] (regarding an IFE in the visible-light regime, see also Supplementary Note 4). Moreover, the different nature of the Gd 4f and Fe 3d magnetic moments with respect to their SOC and predominantly localized vs. itinerant character suggests that comparing element-specific excitation of the rare-earth and transition metal sublattices will contribute to fully revealing the microscopic mechanisms behind the XUV and soft x-ray IFE.

From a more general perspective, our findings reveal an efficient method to transiently generate large macroscopic magnetization on ultrafast time scales. Microscopically rooted in the stimulated Raman scattering process, the XUV-induced IFE demonstrated here can be seen, depending on the helicity of the exciting XUV pulse, to either generate or annihilate a transient magnetization within a range of up to ≈30% of the ground-state magnetization value of ferrimagnetic GdFeCo. Given its strength and robustness, such an opto-magnetic core-level effect is expected to be of relevance for the fields of ultrafast magnetism and spintronics, coherent magnetization control and nonlinear x-ray science. Moreover, touching upon the generality of the effect, the IFE via core-level excitations could essentially be extended to any non-magnetic materials with strong spin-orbit coupling in order to transiently generate a macroscopic magnetic moment.

Methods

Experimental techniques and data acquisition

The time-resolved studies were performed at the DiProI end-station of the FERMI FEL[39], using a pump-probe geometry as schematically shown in Fig. 1a. For simultaneously measuring both the magneto-optical Faraday rotation in transmission and the Kerr rotation in reflection, two polarization-sensitive balanced photodetection schemes were employed. The magnetic contrast was obtained upon flipping an out-of-plane magnetic field of ±8 mT that was magnetically saturating the sample, also restoring the initial magnetization state after each pump-probe cycle. Taking the difference between the two traces recorded for opposite magnetization states leads to a quantity that is directly proportional to the magnetization, as the non-magnetic background cancels out. The experimental time resolution was evaluated to be ≈280 fs, using the method described by Ziolek et al.[40] accounting for the enclosed angle of 45° between pump and probe beams as well as their spatial footprint on the sample. The FEL and optical laser system were operating at 50 Hz repetition rate. The effective repetition rate of the XUV pump was reduced to 25 Hz by seeding only every second electron bunch in the FEL, allowing for an interleaved measurement to record both pumped and unpumped states of the sample. Supplementary Fig. 1 exemplarily shows the data as recorded, i.e., the individually acquired magneto-optical Faraday signals as a function of pump-probe delay. Sorting the data after FEL pulse energy, which was shot-by-shot recorded by an I_0 gas monitor detector, allows retrieving the fluence-dependence (compare Supplementary Fig. 2). For a more extensive technical background about the experimental methods and data acquisition, see Supplementary Notes 1, 2.

Sample design and spectroscopy

The studied sample was a 20 nm thin amorphous film of a ferrimagnetic $Gd_{24}Fe_{67}Co_9$ alloy with an out-of-plane magnetic anisotropy. For static absorption spectroscopy, it was deposited on a 30 nm Si_3N_4 membrane, allowing transmission of the XUV radiation. For the time-resolved measurements, a 1 mm thick glass substrate was used in order to allow simultaneous detection of the Faraday and Kerr signals. In both cases, the magnetic sample was sandwiched between Ta seed and capping layers to protect it from oxidation. The exact sample compositions are Ta(2 nm)/GdFeCo(20 nm)/Ta(5 nm)/Si_3N_4(30 nm) and Ta(2 nm)/GdFeCo(20 nm)/Ta(5 nm)/Glass(1 mm), respectively.

The static XUV absorption and XMCD of the sample shown in Fig. 1b was characterized employing the ALICE reflectometer[41] at the PM3 beamline of BESSY II[42]. The XMCD spectrum thereby corresponds to the asymmetry (A) of the transmitted circularly polarized XUV radiation ($T_{\uparrow,\downarrow}$) measured for opposite magnetic field directions perpendicular to the sample plane, calculated by $A = (T_\uparrow - T_\downarrow) / (T_\uparrow + T_\downarrow)$. For obtaining the XAS ($B_{\uparrow,\downarrow}$), the transmitted XUV intensity was normalized to the beamline spectrum (T_0) by $B_{\uparrow,\downarrow} = -\ln(T_{\uparrow,\downarrow} / T_0)$. For comparison, this characterization was also carried out for a similar $Gd_{24}Fe_{76}$ sample, i.e., without the Co ingredient but otherwise identical composition. The comparison is shown in Supplementary Fig. 8, showing the influence of the small fraction of Co atoms on the XAS and XMCD. To correct for the limited degree of circular polarization approaching the lower photon energy limits of the beamline, the magnetic part $\Delta\beta$ of the absorptive refractive index was calculated from the measured XMCD for the effective thickness of the Fe content within the alloy and normalized to reference XMCD measurements on pure Fe systems[43]. The corrected XMCD magnitude at the Fe $M_{3,2}$ resonance agrees with the values reported in the literature for comparable GdFe systems[44,45].

Atomistic spin dynamics simulations

Atomistic spin dynamics (ASD) simulations were carried out[11] to simulate the influence of the dichroic absorption on the helicity-dependent demagnetization amplitudes. The magnitude of the dichroic absorption was set according to the XMCD asymmetry obtained from the static XUV and XMCD spectroscopy (see Fig. 1b), i.e., (− 6.2 ± 0.5) % in case of 54.1 eV, (− 3.0 ± 0.5) % in case of 56.1 eV and (0.5 ± 0.5) % in case of 51.0 eV excitation, respectively (note that for 64.0 eV, the XMCD is fully zero, thus no dichroic absorption is expected). The resulting simulated fluence-dependencies of the maximum demagnetization amplitudes upon $\sigma_\pm$-polarized excitation are shown in Supplementary Fig. 9 together with their difference ΔM.

Simulating also the dynamics excited by linearly polarized radiation allows better comparability between experiment and simulation by comparing the simulated XMCD-induced and experimentally obtained helicity-dependence ΔM based on the respective fluences that lead to the same amount of demagnetization in the linearly polarized case. Both the experimentally observed (yellow color) and simulated (purple color) ΔM values are shown in Supplementary Fig. 10 as a function of the maximum demagnetization amplitudes induced by linearly polarized excitation of the same fluence. The comparison between experiment and ASD simulations presented in Fig. 4 is based on the largest ΔM observed in the experiment for each XUV photon energy and the interpolated value of ΔM taken from the ASD simulation resembling the respective magnitude of XMCD.

The ASD simulations are done using the VAMPIRE software package[33,34] based on the Landau-Lifshitz-Gilbert (LLG) equation. The system Hamiltonian is given by:

$$\mathcal{H} = -\sum_{i<j}(\mathbf{S}_i\,\mathbf{J}_{ij}\,\mathbf{S}_j) - k_\mathrm{u}\sum_i(\mathbf{S}_i\cdot\mathbf{e})^2 \qquad (2)$$

where $\mathbf{S}_i$, $\mathbf{S}_j$ are the normalized spin vectors on i, j sites, $\mathbf{J}_{ij}$ is the exchange constant and k_u is the uniaxial magnetocrystalline anisotropy energy constant per site. We used similar parametrization as reported in literature[12,35]: $\mu_\mathrm{Fe} = 1.92\mu_\mathrm{B}$ and $\mu_\mathrm{Gd} = 7.63\mu_\mathrm{B}$, the anisotropy is taken as

$k_u = 8.07246 \cdot 10^{-24}$ J and the exchange interactions are $J_{Fe\text{-}Fe} = 2.835 \cdot 10^{-21}$ J, $J_{Gd\text{-}Gd} = 1.26 \cdot 10^{-21}$ J and $J_{Fe\text{-}Gd} = -1.09 \cdot 10^{-21}$ J. We incorporate the rapid change in thermal energy of a system under the influence of a femtosecond laser pulse using the two-temperature model[46]:

$$\begin{aligned} T_e C_e \frac{dT_e(t)}{dt} &= -G_{e-ph}[T_{ph}(t) - T_e(t)] + P_{abs}(t), \\ C_{ph} \frac{dT_{ph}(t)}{dt} &= G_{e-ph}[T_e(t) - T_{ph}(t)], \end{aligned} \tag{3}$$

where $C_e = 225$ $Jm^{-3}K^{-2}$, $C_{ph} = 3.1 \cdot 10^6$ $Jm^{-3}K^{-1}$ and $G_{e\text{-}ph} = 2.5 \cdot 10^{17}$ $Wm^{-3}K^{-1}$. The spin system is coupled to the electron temperature T_e and the quantity $P_{abs}(t)$ corresponds to the laser power density absorbed by the electronic system and depends on laser fluence and light polarization. The XMCD effect is included by modifying $P_{abs}(t)$ proportional to the percentage obtained from the experiments.

Ab initio calculations of the inverse Faraday effect

The ab initio calculations of the IFE were carried out using the second-order response theory formalism as derived by Berritta et al.[6] and Battiato et al.[8]. The calculations were performed with the full-potential, all-electron code WIEN2k[47], with spin-orbit interaction included.

The system was modeled as a stoichiometric $GdFe_2Co$ unit cell in the $AuCu_3$ structure, i.e., as $GdFe_3$, but with one Fe atom replaced by Co. The lattice parameters were first optimized using the VASP code[48], after which the electronic structure and IFE was computed with the WIEN2k program. To capture the strong electron correlations in the Gd 4f shell, we employed the GGA + U method, in the atomic limit version, with parameters $U = 7$ eV and $J = 1$ eV, in combination with the generalized gradient approximation (GGA)[49] to the exchange-correlation potential. The calculated band structure is shown in Supplementary Fig. 11. The occupied Gd 4f states are located at −6 eV and the unoccupied 4f states start at +4 eV. The spin-polarized Fe and Co 3d states that are accessed by XUV photon excitation of the 3p states are in the energy window of 0 to 4 eV.

To compute the IFE, the exchange splitting of the 3p semi-core states of Fe and Co atoms was included as well[50]. The computed opto-magnetic IFE response is shown in Supplementary Fig. 12. The photon energy- and helicity-dependent IFE constants are given for the total optically induced magnetization M_{ind}, i.e., they contain both spin and orbital contributions (see Berritta et al.[6]). The IFE constants for σ_- and σ_+ circular polarizations are clearly distinct in the photon energy range of the Fe and Co M absorption edges while for energies outside of this range the distinction between σ_- and σ_+ polarizations vanishes. The bottom panel of Supplementary Fig. 12 shows Δ_{IFE}, i.e., the difference between the opto-magnetic constants for the two helicities. To understand this spectrum, we can first note that, in the absence of spin magnetization in the alloy, the IFE spectra for σ_- and σ_+ polarizations would be identical but with opposite sign. This feature can be approximately recognized in Supplementary Fig. 12. When there is spin magnetization present, the exchange splitting of the 3d valence bands leads to an energy-dependent shift in the individual IFE spectra, such that $\mathcal{K}^{IFE}_{\sigma_+}(\omega) \neq -\mathcal{K}^{IFE}_{\sigma_-}(\omega)$. A pronounced difference between $\mathcal{K}^{IFE}_{\sigma_+}(\omega)$ and $-\mathcal{K}^{IFE}_{\sigma_-}(\omega)$ occurs at $53 - 55$ eV (top panel of Supplementary Fig. 12), i.e., where the $3p \rightarrow 3d$ resonance occurs for Fe in the calculations. Around $58 - 60$ eV, a similar difference is expected to appear near the Co 3p absorption edge. However, there will be an overlap of the M edges of Fe and Co in this photon energy range which can partially cancel out each other. In addition, we mention that previously, it was found that the ab initio computed XUV spectra of 3d transition metals compared well with measured spectra, but the computed energy onset of the $M_{3,2}$ edge differs from the measured onset position by about 2.5 eV[30–32]. This difference occurs because the ab initio calculated energy positions of the semi-core levels can deviate from the real energy positions and, in addition, there is an effect of the core hole in the XUV excitation which can lead to a shift in the binding energy of the semi-core levels[30,50]. The Δ_{IFE} spectrum shown in Fig. 4 has therefore been shifted by +2.5 eV to align with the experimental onset of the Fe M edge, which precisely corresponds to the shift that has been used in previous work[32]. We remark further that the computed IFE spectrum is valid in the quasi-static approximation, i.e., assuming that the computed IFE response is modulated only by the envelope of the XUV pulse. The employed second-order response theory is furthermore expected to be valid for reasonable, but not too high laser fluences.

Data availability

The raw data were generated at the FERMI free-electron laser (DiProI end-station) and BESSY II synchrotron radiation (PM3 beamline) facilities. All data needed to evaluate the conclusions of this study are presented in the main article and/or the Supplementary Information, and are available from the corresponding authors upon request.

Received: 25 October 2023; Accepted: 4 June 2024;
Published online: 14 June 2024

References

1. Kirilyuk, A., Kimel, A. V. & Rasing, T. Ultrafast optical manipulation of magnetic order. *Rev. Mod. Phys.* **82**, 2731–2784 (2010).
2. Carva, K., Baláž, P. & Radu, I. Chapter 2 - Laser-Induced Ultrafast Magnetic Phenomena. in *Handbook of Magnetic Materials* (ed. Brück, E.) **26** 291–463 (Elsevier, 2017).
3. Siegrist, F. et al. Light-wave dynamic control of magnetism. *Nature* **571**, 240–244 (2019).
4. Lloyd-Hughes, J. et al. The 2021 ultrafast spectroscopic probes of condensed matter roadmap. *J. Phys. Condens. Matter* **33**, 353001 (2021).
5. van der Ziel, J. P., Pershan, P. S. & Malmstrom, L. D. Optically-induced magnetization resulting from the inverse faraday effect. *Phys. Rev. Lett.* **15**, 190–193 (1965).
6. Berritta, M., Mondal, R., Carva, K. & Oppeneer, P. M. Ab initio theory of coherent laser-induced magnetization in metals. *Phys. Rev. Lett.* **117**, 137203 (2016).
7. Battiato, M., Barbalinardo, G., Carva, K. & Oppeneer, P. M. Beyond linear response theory for intensive light-matter interactions: Order formalism and ultrafast transient dynamics. *Phys. Rev. B* **85**, 045117 (2012).
8. Battiato, M., Barbalinardo, G. & Oppeneer, P. M. Quantum theory of the inverse Faraday effect. *Phys. Rev. B* **89**, 014413 (2014).
9. Stanciu, C. D. et al. Ultrafast interaction of the angular momentum of photons with spins in the metallic amorphous alloy GdFeCo. *Phys. Rev. Lett.* **98**, 207401 (2007).
10. Stanciu, C. D. et al. All-optical magnetic recording with circularly polarized light. *Phys. Rev. Lett.* **99**, 047601 (2007).
11. Radu, I. et al. Transient ferromagnetic-like state mediating ultrafast reversal of antiferromagnetically coupled spins. *Nature* **472**, 205–208 (2011).
12. Ostler, T. A. et al. Ultrafast heating as a sufficient stimulus for magnetization reversal in a ferrimagnet. *Nat. Commun.* **3**, 666 (2012).
13. Vahaplar, K. et al. All-optical magnetization reversal by circularly polarized laser pulses: Experiment and multiscale modeling. *Phys. Rev. B* **85**, 104402 (2012).
14. Scheid, P., Remy, Q., Lebègue, S., Malinowski, G. & Mangin, S. Light induced ultrafast magnetization dynamics in metallic compounds. *J. Magn. Magn. Mater.* **560**, 169596 (2022).
15. Popova, D., Bringer, A. & Blügel, S. Theory of the inverse Faraday effect in view of ultrafast magnetization experiments. *Phys. Rev. B* **84**, 214421 (2011).
16. Freimuth, F., Blügel, S. & Mokrousov, Y. Laser-induced torques in metallic ferromagnets. *Phys. Rev. B* **94**, 144432 (2016).
17. Freimuth, F., Blügel, S. & Mokrousov, Y. Laser-induced torques in metallic antiferromagnets. *Phys. Rev. B* **103**, 174429 (2021).

18. Scheid, P., Sharma, S., Malinowski, G., Mangin, S. & Lebègue, S. Ab initio study of helicity-dependent light-induced demagnetization: from the optical regime to the extreme ultraviolet regime. *Nano Lett.* **21**, 1943–1947 (2021).
19. Vijayakumar, M. & Gopinathan, M. S. Spin-orbit coupling constants of transition metal atoms and ions in density functional theory. *J. Mol. Struct. THEOCHEM* **361**, 15–19 (1996).
20. Lutman, A. A. et al. Polarization control in an X-ray free-electron laser. *Nat. Photonics* **10**, 468–472 (2016).
21. Higley, D. J. et al. Femtosecond X-ray induced changes of the electronic and magnetic response of solids from electron redistribution. *Nat. Commun.* **10**, 5289 (2019).
22. Schneider, M. et al. Ultrafast demagnetization dominates fluence dependence of magnetic scattering at Co M edges. *Phys. Rev. Lett.* **125**, 127201 (2020).
23. Serkez, S. et al. Opportunities for Two-Color Experiments in the Soft X-ray Regime at the European XFEL. *Appl. Sci.* **10**, 2728 (2020).
24. Liu, X. et al. Sub-15-fs X-ray pump and X-ray probe experiment for the study of ultrafast magnetization dynamics in ferromagnetic alloys. *Opt. Express* **29**, 32388–32403 (2021).
25. Yao, K. et al. Distinct spectral response in M-edge magnetic circular dichroism. *Phys. Rev. B* **102**, 100405(R) (2020).
26. Hennes, M. et al. Time-Resolved XUV Absorption Spectroscopy and Magnetic Circular Dichroism at the Ni $M_{2,3}$-Edges. *Appl. Sci.* **11**, 325 (2021).
27. Kimel, A. V. et al. Ultrafast non-thermal control of magnetization by instantaneous photomagnetic pulses. *Nature* **435**, 655–657 (2005).
28. Hansteen, F., Kimel, A., Kirilyuk, A. & Rasing, T. Nonthermal ultrafast optical control of the magnetization in garnet films. *Phys. Rev. B* **73**, 014421 (2006).
29. John, R. et al. Magnetisation switching of FePt nanoparticle recording medium by femtosecond laser pulses. *Sci. Rep.* **7**, 4114 (2017).
30. Turgut, E. et al. Stoner versus Heisenberg: Ultrafast exchange reduction and magnon generation during laser-induced demagnetization. *Phys. Rev. B* **94**, 220408(R) (2016).
31. Zusin, D. et al. Direct measurement of the static and transient magneto-optical permittivity of cobalt across the entire M-edge in reflection geometry by use of polarization scanning. *Phys. Rev. B* **97**, 024433 (2018).
32. Vaskivskyi, I. et al. Element-Specific Magnetization Dynamics in Co–Pt Alloys Induced by Strong Optical Excitation. *J. Phys. Chem. C.* **125**, 11714–11721 (2021).
33. Evans, R. F. L. et al. Atomistic spin model simulations of magnetic nanomaterials. *J. Phys. Condens. Matter* **26**, 103202 (2014).
34. Vampire software package, Version 5. https://vampire.york.ac.uk/.
35. Iacocca, E. et al. Spin-current-mediated rapid magnon localisation and coalescence after ultrafast optical pumping of ferrimagnetic alloys. *Nat. Commun.* **10**, 1756 (2019).
36. Abela, R. et al. The SwissFEL soft X-ray free-electron laser beamline: Athos. *J. Synchrotron Radiat.* **26**, 1073–1084 (2019).
37. Wei, T., Li, P., Li, Y. & Pflueger, J. Radiation properties of the SASE3 afterburner for European XFEL. in *Advances in X-ray Free-Electron Lasers Instrumentation IV* (eds. Tschentscher, T. & Patthey, L.) **10237** 67–74 (SPIE, 2017).
38. Khorsand, A. R. et al. Role of magnetic circular dichroism in all-optical magnetic recording. *Phys. Rev. Lett.* **108**, 127205 (2012).
39. Capotondi, F. et al. Multipurpose end-station for coherent diffraction imaging and scattering at FERMI@Elettra free-electron laser facility. *J. Synchrotron Radiat.* **22**, 544–552 (2015).
40. Ziolek, M. et al. The influence of the excitation geometry on the temporal resolution in femtosecond pump–probe experiments. *Opt. Commun.* **197**, 467–473 (2001).
41. Abrudan, R. et al. ALICE—An advanced reflectometer for static and dynamic experiments in magnetism at synchrotron radiation facilities. *Rev. Sci. Instrum.* **86**, 063902 (2015).
42. Kachel, T., Eggenstein, F. & Follath, R. A soft X-ray plane-grating monochromator optimized for elliptical dipole radiation from modern sources. *J. Synchrotron Radiat.* **22**, 1301–1305 (2015).
43. Willems, F. et al. Magneto-Optical Functions at the 3p Resonances of Fe, Co, and Ni: Ab initio Description and Experiment. *Phys. Rev. Lett.* **122**, 217202 (2019).
44. von Korff Schmising, C. et al. Element-Specific Magnetization Dynamics of Complex Magnetic Systems Probed by Ultrafast Magneto-Optical Spectroscopy. *Appl. Sci.* **10**, 7580 (2020).
45. Hessing, P. Interference-based spectroscopy with XUV radiation. (Technische Universität Berlin, Berlin, 2021). https://doi.org/10.14279/depositonce-11864.
46. Jiang, L. & Tsai, H.-L. Improved Two-Temperature Model and Its Application in Ultrashort Laser Heating of Metal Films. *J. Heat. Transf.* **127**, 1167–1173 (2005).
47. Blaha, P. et al. *WIEN2k, An Augmented Plane Wave + Local Orbitals Program for Calculating Crystal Properties*. (Karlheinz Schwarz, Techn. Universität Wien, Austria, 2018).
48. Kresse, G. & Furthmüller, J. Efficiency of ab-initio total energy calculations for metals and semiconductors using a plane-wave basis set. *Comput. Mater. Sci.* **6**, 15–50 (1996).
49. Perdew, J. P., Burke, K. & Ernzerhof, M. Generalized Gradient Approximation Made Simple. *Phys. Rev. Lett.* **77**, 3865–3868 (1996).
50. Valencia, S. et al. Quadratic X-Ray Magneto-Optical Effect upon Reflection in a Near-Normal-Incidence Configuration at the M Edges of 3d-Transition Metals. *Phys. Rev. Lett.* **104**, 187401 (2010).

Acknowledgements

I.R. acknowledges funding from the Federal Ministry of Education and Research (BMBF) through project 05K16BCA (Femto-THz-X) and the European Research Council through project TERAMAG (Grant No. 681917). C.v.K.S., P.M.O. and S.E. would like to thank the German Research Foundation (DFG) for funding through CRC/TRR 227 projects A02 and MF (project ID 328545488). S.R. gratefully acknowledges the support of ARCHER UK National Supercomputing Service via the project e733. S.R. and T.O. gratefully acknowledge the financial support from the EPSRC TERASWITCH project (project ID EP/T027916/1). L.S. and P.M.O. acknowledge support by the Swedish Research Council (VR), the K. and A. Wallenberg Foundation (Grants No. 2022.0079 and 2023.0336), and the European Union's Horizon 2020 Research and Innovation Programme under FET-OPEN Grant Agreement No. 863155 (s-Nebula). Part of the calculations were provided by the Swedish National Infrastructure for Computing (SNIC), funded by VR through grant No. 2018-05973. The authors acknowledge Elettra Sincrotrone Trieste for providing access to its free-electron laser facilities and thank all members of the different departments at FERMI for their outstanding assistance during the preparation and realization of the experiment. The authors also thank the Helmholtz-Zentrum Berlin für Materialien und Energie for the allocation of synchrotron-radiation beamtime.

Author contributions

I.R. conceived the original experimental idea. M.H. and I.R. conceived the experiment. The time-resolved measurements were prepared and performed by M.H., I.R., C.v.K.S., K.Y., E.J., B.V., V.C., K.L., F.C., D.N., E.P. and I.L.Q., I.P.N., L.R. and G.D.N. helped setting up the experiment. On-site data monitoring was performed by M.H., K.Y., K.L. and F.C., D.E. prepared and optimized the samples, M.H. carried out the static sample characterization. The data treatment and analysis was performed by M.H. with contributions from I.R. and F.C., L.S. and P.M.O developed the IFE theory and carried out the ab initio calculations. S.R., R.C. and T.O. performed the ASD simulations. C.v.K.S., B.P. and S.E. contributed to the discussion and interpretation of the results. The manuscript was written by M.H. and I.R. with contributions from S.R. and P.M.O. All authors commented on the manuscript.

Funding
Open Access funding enabled and organized by Projekt DEAL.

Competing interests
The authors declare no competing interests.

Additional information
Supplementary information The online version contains supplementary material available at https://doi.org/10.1038/s42005-024-01686-7.

Correspondence and requests for materials should be addressed to Martin Hennecke or Ilie Radu.

Peer review information *Communications Physics* thanks Roopali Kukreja, Manfred Fiebig and the other, anonymous, reviewer(s) for their contribution to the peer review of this work.